Journal of Environmental Chemical Engineering 12 (2024) 114589

Contents lists available at ScienceDirect

Journal of Environmental Chemical Engineering

journal homepage: www.elsevier.com/locate/jece

Activation of volcanic ash as support for FeO_x gliding arc plasma deposition and application in the catalytic oxidation of Rhodamine 6 G

Mélanie Pitap-Mbowou [a], Franck W. Boyom-Tatchemo [a,*], Elie Acayanka [a], Georges Kamgang-Youbi [a], Christophe Poupin [b], Sebastián A. Gámez-Rivera [c], Renaud Cousin [b], Eric M. Gaigneaux [c], Samuel Laminsi [a,*]

[a] University of Yaounde I, Faculty of Science, Department of Inorganic Chemistry, Cameroon
[b] Université du Littoral Côte d'Opale, Unité de Chimie Environnementale et Interactions sur le Vivant, UR4492, 145 Avenue Maurice Schumann, Dunkerque 59140, France
[c] Université catholique de Louvain, Institute of Condensed Mater and Nanosciences-IMCN, Division "Molecular Chemistry, Materials and Catalysis-MOST", Place Louis Pasteur 1/L4.01.09.1348 Louvain -la Neuve, Belgium

ARTICLE INFO

Keywords:
Iron oxides
Volcanic ash
Plasma-precipitation
Heterogeneous Fenton
Supported catalyst
Hetero-structure
Plasma-Liquid/solid interactions

ABSTRACT

This study reports the chemical activation of volcanic ash (VA), a local material to promote the subsequent deposition of FeO_x nanoparticles through a gliding arc plasma-assisted route to obtain an efficient Fenton catalyst for a better degradation of Rhodamine 6 G in aqueous solution. Plasma-oxidation of Fe(II) solution within the pores of activated VA was performed, then followed the maturation of crystallites (deposited precipitated) thanks to plasma post-discharge species. The obtained materials were characterized by Fourier- Transform Infrared transmission spectroscopy (FTIR), X-ray diffraction (XRD), Nitrogen Physisorption, Thermogravimetric analyses, Scanning electron microscopy (SEM) and Energy Dispersive X-ray spectroscopy (EDX). The acid activation of volcanic ash for 2 h (AM-2) using H_2SO_4 solution, followed by gliding arc plasma-assisted hydrolytic precipitation of Iron oxide during 30 min (AM-FeO_x-30/0) significantly decreased the size of agglomerates particles of VA, leading to the increase by two orders the magnitude the total pore volume as well as the specific surface area. SEM and EDX analyses attested to the incorporation of Fe within the activated volcanic ash framework. The studies also show that plasma-deposited iron oxide nanoparticles are located within different phases of VA. For the obtained AM-FeO_x-30/0 material after 30 min of gliding arc plasma deposition on activated VA, Iron oxides are located within the Augite and Goethite phases. While, for the material obtained after plasma-deposition (30 min) followed by ageing at 100°C through a water boiling bath for 4 h (AM-FeO_x-30/4), Iron oxides are located within sodium Diopside and Goethite phases. Fenton catalytic activity of the different materials was evaluated for degradation of Rhodamine 6 G and revealed degradation degrees of 31, 95, 79, and 80 % respectively for VA, AM-2, AM-FeO_x-0/2 and AM-FeO_x-30/4 in the optimum condition (t=20 min, pH=7, [catalyst]=3 g/L, [Rh6G] = 25 mg/L, 1 mL of H_2O_2 at 30 %. Recyclability tests confirmed the stable catalytic activity of plasma-supported material after 4 runs. These results highlight the valorisation of volcanic ash for the improvement of Fenton catalytic degradation of organic pollutants in solution.

1. Introduction

In recent years, Fenton's heterogeneous catalysis has been one of the most popular advanced oxidation processes for the degradation of industrial organic pollutants [1–4]. This process is based on the production of hydroxyl radicals (HO) as powerful oxidizing species through the catalysed decomposition of hydrogen peroxide by a solid catalyst rich in iron, which species thus leads to the degradation (mineralization) of the organic pollutant Eqs. (1–3) [5,6].

$$\equiv Fe^{3+} + H_2O_2 \rightarrow \equiv Fe^{2+} + HOO^{\cdot} + H^{+} \quad (1)$$

$$\equiv Fe^{2+} + H^{+} + H_2O_2 \rightarrow \equiv Fe^{3+} + HO^{\cdot} + H_2O \quad (2)$$

$$Pollutant + HO^{\cdot} \rightarrow CO_2 + H_2O + Other\ mineralization\ products \quad (3)$$

* Corresponding authors.
E-mail addresses: boyom.william@yahoo.com (F.W. Boyom-Tatchemo), samuellaminsi@gmail.com (S. Laminsi).

https://doi.org/10.1016/j.jece.2024.114589
Received 20 August 2024; Received in revised form 17 October 2024; Accepted 27 October 2024
Available online 29 October 2024

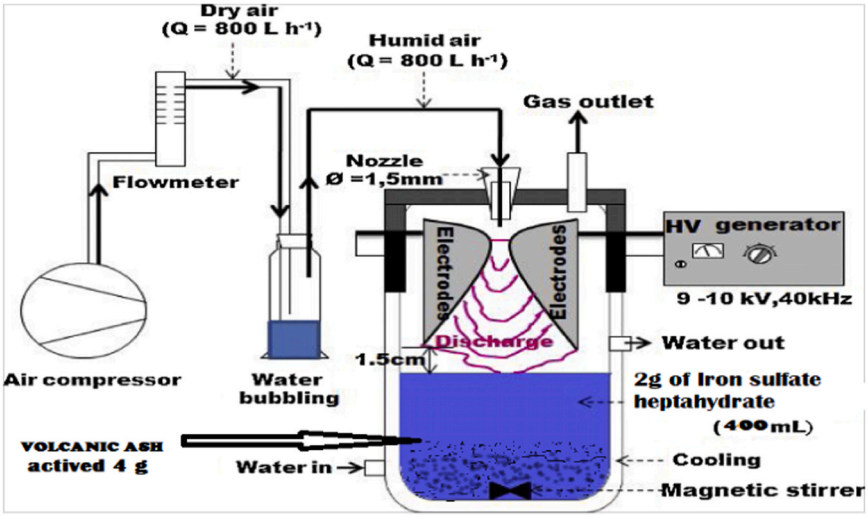

Fig. 1. Experimental setup of glidarc plasma route.

(Where ≡ represents the surface of the solid catalyst where iron is located)

This widely used method is interesting because of its simplicity, low cost of implementation, and the possibility of the catalyst recycling. However, the heterogeneous Fenton catalysis was set up to overcome the problem of sludge formation that requires a second treatment, and the large quantities of iron that leach at low pH during homogeneous Fenton catalysis [7]. Why researchers are focusing their attention on the synthesis of solid iron-based catalysts for an efficient Fenton catalytic process. It has been reported that the deposition of iron particles on micro-sized materials such as zeolites, clays, sand, laterite or activated carbons leads to the obtaining of a good heterogeneous Fenton catalyst easily recyclable [8]. Additionally, it was also proven that natural materials rich in aluminosilicate are good catalytic carriers, thus allowing a good dispersion of iron oxides on their surfaces and preventing the leaching of iron during catalytic process in solution. Therefore, some authors have developed various techniques for the preparation of Fenton catalysts using clay materials very rich in alumina and silica. Tarkwa et al., calcined laterite at 400°C to get goethite and hematite for photocatalytic degradation of Orange II [9]. Hassan and Hamed performed the preparation by impregnation of the Iron-Ball for the heterogeneous Fenton degradation of the blue reagent 4 [10]. Fida et al., also prepared via simple precipitation method the Montmorillonite La-Fer for the degradation of Rhodamine B and Methylene Blue [11]. Lim et al., obtained active heterogeneous Fenton catalysts through the impregnation of iron oxide nanoparticles on alumina-coated mesoporous SBA-15 silica [12]. Qian et al., dispersed amorphous FeOOH on g-C_3N_4 as photo Fenton catalyst for degradation of recalcitrant organic pollutants [13]. Unfortunately, most of these classical synthesis methods show some drawbacks including the long preparation times, use of strong bases for precipitation and organics surfactants in some cases, thus high costs of implementing impregnation and pillarization processes [6]. Why the development of new efficient and environmentally friendly technique, has become urgent. Gliding arc plasma (plasma glidarc) route appears as an effective deposition method, considering its interesting redox properties, operating at ambient conditions, and very simple to be implemented. Recently, Miloh et al., reported the enhancement of the Fenton reactions via plasma glidarc supported magnetite (Fe_3O_4) nanoparticles on water hyacinth biomass fibber [5]. Here, we intend to use volcanic ash (VA) as a cost-free local material rich in aluminosilicates [14–16]. This ash is very abundant worldwide and is made up of aluminium oxide, iron oxide, silicon oxide, titanium oxide, and others, which makes it very attractive for several applications such as catalysis [17,18]. In our previous work, we showed that the use of 5 g/L of volcanic ash with 400 µm as granulometry, containing 13 % Iron oxide could degrade up to 80 % of Rhodamine 6 G (25 mg/L) dye after 120 minutes of Fenton catalytic treatment [7]. This dye is known for its recalcitrant and carcinogenic character and has been declared environmentally toxic [19]. To reach a high degradation of this pollutant in short exposure times and low catalyst concentration, volcanic ash material requires additional treatment to improve its physicochemical properties.

In this study, the volcanic ash is modified by acid activation to increase its specific surface area and porosity, and then used as a porous framework for the hydrolytic precipitation of FeO_x nanoparticles through the plasma glidarc route as an innovative and green method, to reinforce the heterogeneous Fenton catalytic performance of the material. The specificity of plasma glidarc as non-thermal plasma lies in the large production of visible-ultraviolet light and active chemical species such as $O^{\cdot}$, O_3, $HO^{\cdot}$, H_2O_2, $NO^{\cdot}$, $N^{\cdot}$, N_2*, NO_2^- and NO_3^- without the use of chemical reagents [20–22]. The effect of post-discharge plasma species on the maturation of crystallites has been explored. The prepared materials will be applied for the degradation of Rhodamine 6 G as a pollutant model to evaluate and compare their catalytic performance and recyclability.

2. Material and method

2.1. Material

The volcanic ash (VA) used in this work was provided by the MIPROMALO (Mission for the Promotion of Local Materials in Cameroon) at Foumbot in the Western Region of Cameroon. Rhodamine 6 G (Fig. S1) was purchased from Sigma-Aldrich in Belgium and used without purification. This synthetic azo dye 9-[2-(ethoxycarbonyl) phenyl] −3,6-bis(ethylamino)-2,7-dimethylxanthylium chloride of the xanthene family has an intense peak at 513 nm, characteristic of the chromophore components (aromatic rings connected by azo groups) responsible of its coloration and its approximate dimensions are given in Figure S1 [23]. Sodium hydroxide (NaOH, 100 %) and sulphuric acid (H_2SO_4, 98 %) were purchased at Sigma-Aldrich company, while hydrogen peroxide (H_2O_2, 50 %) and heptahydrated iron sulphate were purchased at Merck company.

2.2. Preparation of catalyst

Volcanic Ash was washed several times with deionized water to remove soluble impurities and then dried at room temperature for three days. The cleaned material was crushed and sieved using a 100 µm sieve

(instead of 400μm as in the previous work because the decreasing particle sizes increase the specific surface area and the reactivity of the material Figure S2 [24,25]). Afterward, the chemical activation was performed by mixing 100 mL of sulphuric acid (3 M) with 10 g of washed and sieved volcanic ash into the boiling water bath (100°C) under mechanical stirring at 500 rpm. The treatment was carried out for 2 hours, and the resulting material was vacuum-filtered, washed with hot distilled water to reach neutral pH, dried in an oven at 105°C for 3 hours, and named AM-2.

The nanocomposite was synthesized through the gliding arc plasma-assisted hydrolytic precipitation technique (Fig. 1). For this purpose, 0.2 g of Iron Sulphate Heptahydrate ($FeSO_4.7H_2O$) was dissolved in 400 mL of distilled water to obtain 0.5 g/l of Iron (II) solution and mixed with 4 g of activated volcanic ash (AM-2). Then, after 30 min of dispersion using a magnetic stirrer (Figure S3a), the suspension was exposed to glidarc-type plasma discharge for 30 minutes. A yellow-brown precipitate was obtained via plasma-oxidation of Fe (II) solution (Figure S3b), then a part of this suspension was collected, washed with distilled water and dried in oven at 105°C for 24 h and the resulting compound was named AM-FeO_x-30/0. While the other part of the suspension was exposed to ageing within a boiling water bath (100°C) for 4 hours under mechanical agitation to pursue the crystallization. (Figure S3c). The aged material was collected, washed, dried in an oven for 24 h at 105°C and the resulting composite was named AM-FeO_x-30/4.This ageing is carried out at 100°C instead of ambient temperature (25°C) to avoid the agglomeration and contaminating phase which induces the inactivity of the prepared catalyst [22].

2.3. Characterization of obtained materials

Fourier Transform Infrared spectroscopy was performed to collect information on the different functional group's components of each material. It was performed with Perkin Elmer Frontier ATR ALPHABRUKER device. Each spectrum was obtained from 4000 to 600 cm^{-1} after 32 scans with a resolution of 4 cm^{-1}. All samples were scanned five times and the average of these spectra was scrutinized between 1800 and 600 cm^{-1}. XRD analyses were performed between 5 and 80° in 2θ with a step of 0.02° every 2 s, using a Bruker AXS Advance D8 device, and Cu source (λ=0.15418 nm) of which the K-alpha2 line was removed, and a LynxEye XT detector. The operations were made with a search for the elements Ca, Al, Si, O, Mg, Fe and Ti. For nitrogen physisorption, a vacuum pre-treatment was done at 150 °C for 12 h before the analysis of each sample. Analyses were performed using a Micromeritics analyzer by adsorption of nitrogen (N_2) at a temperature of 77 K, and a relative pressure P/P° ranging from 0 to 0.98. Adsorption-desorption isotherms were used to determine the specific surface area by applying the classical Brunauer, Emmet, and Teller (BET) method. The Barrett-Joyner-Halenda (BJH) method was used to determine the pore size distribution from the desorption branch. The microporous volume and non-porous surface were obtained by the t-plot method of Boer et al. [26]. TGA analysis was carried out on a Mettler Toledo TGA/SDTA 851 TA Instruments SDT 290 thermo-analyzer, in air (100 mL/min) in the temperature range of 25–900°C, at a heating rate of 10°C. SEM and EDX analyses have been performed, respectively to investigate the morphology and get the elemental chemical composition of each material, using a LEO 983 GEMINI electron microscope operated at an acceleration voltage 2 kV. Before analysis, a small quantity of powder from each material is placed on adhesive carbon film which is itself deposited on an aluminium support. Then, 8 nm layer of chromium or gold is sputtered under vacuum with a sputter Metal 208HR (Cressington). The elementary composition of each material was calculated by removing the carbon and chromium (or gold) contribution, and then calculating the average of the analyses at three different points carried out for each sample. All remaining percentages are then brought back to 100 %.

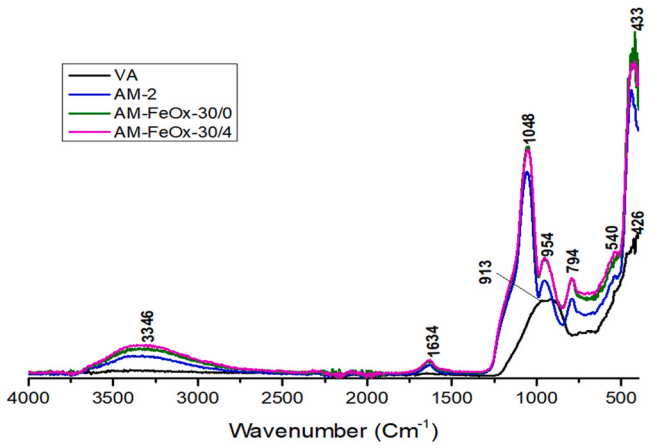

Fig. 2. Infrared spectra of raw material (VA), activated material 2 H (AM-2), supported material (AM-FeOx-30/0), and supported and aged material (AM-FeOx-30/4).

2.4. Catalytic activity of different materials

For each catalytic treatment, a fixed concentration (25 mg/L) of Rhodamine 6 G solution was prepared and adjusted to a suitable pH using sulphuric acid (0.1 M) or sodium hydroxide (0.1 M) solutions. After stirring with a HEIDOLPH magnetic stirrer, the reaction was triggered under mild conditions at 25 ± 3 °C by adding a defined quantity of catalyst and 1 mL of 30 % H_2O_2 given to 100 mL beaker in the presence of daylight. At defined times, volumes of 2 mL of solution were withdrawn and filtered with 0.4 μm membrane filters. The resulting filtrate was analyzed using a spectrophotometer at a wavelength of 513 nm (which corresponds to the absorbance peak of Rh6G). Each test was repeated three times for good accuracy and reproducibility of data. A post-treatment of catalytic degradation of Rhodamine 6 G under optimal conditions was carried out to better assess the elimination process (adsorption and degradation) of pollutant in aqueous solution. For this purpose, the Rhodamine-6G solutions treated under the experimental conditions (t=20 min, m=3 g/L, [Rh-6G]= 25 mg/L, pH=7 and 1 mL of H_2O_2) with the different materials, namely VA, AM-2, AM-FeO_x-30/0 or AM-FeO_x-30/4 were filtered, exposed to the post-catalytic treatment for 24 and 48 hours and analysed by the spectrophotometer. The degradation degree of Rh6G was determined by the Eq. 4.

$$T\% = \frac{C_0 - C_f}{C_0} * 100 \quad (4)$$

C_0: Initial concentration of the pollutant
C_f: Residual concentration after a defined treatment time
T%: Degradation degree of the pollutant

The catalytic stability of the prepared materials was evaluated during four runs, by recovering via filtration the material after each catalytic degradation run of the Rhodamine 6 G under the optimal conditions. The recovered material was washed using distilled water and dried in the oven for 3 hours at 105°C, before next catalytic run. The leaching test was carried out to evaluate the eventual dissolution of iron (bi- and trivalent as well as colloidal iron (III) hydroxides) in solution, and to better appreciate the stability of the catalyst. The test consisted in using Fe-1 reagent Spectroquant (1.14761.0001). Precisely, 5 mL of the solution was withdrawn and introduced in a tube, 3 drops Fe-1 reagent were then added, then the mixture was stirred and left for 3 min. The mixture was finally analysed by spectrophotometry at 565 nm. The untreated Rhodamine 6 G solutions, which means the one that was not exposed to catalytic treatment has been used as a reference solution.

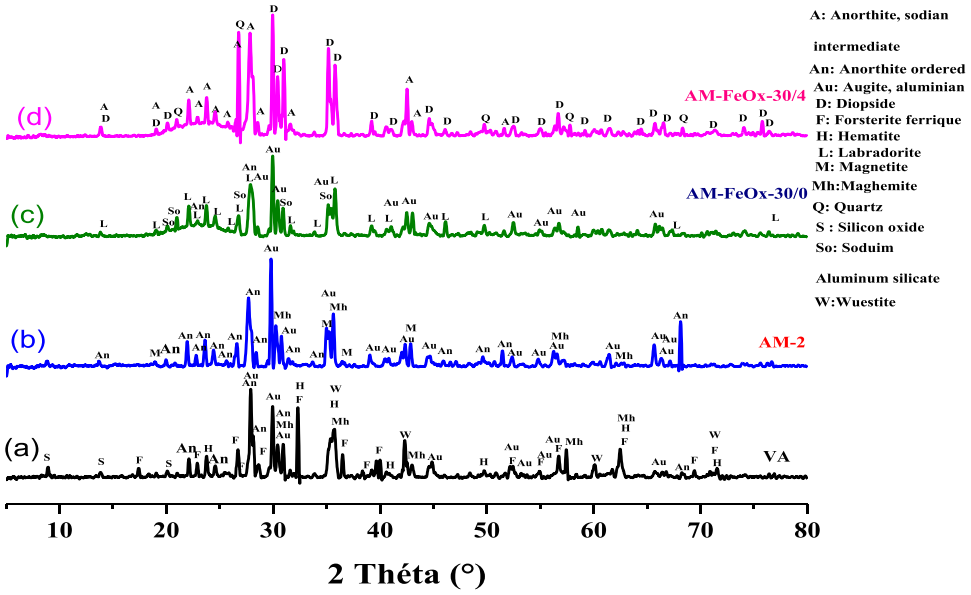

Fig. 3. XRD patterns of (a) Raw (VA), (b) Activated (AM-2), (c) Supported (AM-FeOx-30/0), (d) Ageing (AM-FeOx-30/4) materials.

3. Results and discussion

3.1. Characterization of prepared catalysts

Fig. 2 shows the Fourier Transform Infrared spectra of prepared materials. The raw material (volcanic ash) shows absorption bands at 3401 and 1645 cm^{-1} which are respectively assigned to the stretching and bending vibrations of the O-H bond of water [27]. A wide absorption band around 913 cm^{-1} expresses the symmetrical stretching vibration of the Si-O-T bonds (with T = Si, Al) [10,28]. The bands around 734 and 686 cm^{-1} are assigned to the vibration of the Si-O-Si bond within the SiO_4 tetrahedron [29], while absorption band around 426 cm^{-1} describes the vibrations of the Si-O-Fe bonds [30]. On the activated material (AM-2) spectrum, new absorption bands appear (Fig. 2), reflecting the acidic modification of the volcanic ash (VA) network by protonation and leaching of the SiO_4^- and $(AlO_4)^{5-}$ groups. We observe the intensification of the band around 3346 cm^{-1}, attributed to the stretching O-H vibrations of silanol and aluminol groups and within water molecules already existing in the raw material (VA). While the one at 1634 cm^{-1} is ascribed to the bending vibrations of water molecules. Those around 1057 and 954 cm^{-1} correspond to the vibration mode of Si-O-T bonds (T= Si, Al, Fe), and displacement of wavenumber from 913 cm^{-1} to higher values is explained by geo-polymerization induced by the partial replacement of the SiO_4^- tetrahedra by AlO_4^- tetrahedra within the volcanic ash framework [31]. At 793 cm^{-1}, a vibration mode of α-Fe-O-OH bond of goethite is observed [9,31]. According to the hypotheses put forward by Yannick Cudennec et al. on the formation conditions of α-FeO(OH), it is reported that sulphate ions would decrease the oxidation rate of iron, thus directing the reactions towards the formation of goethite [32]. The band around 540 cm^{-1} corresponds to the vibration mode of Al-O bond with Al in VI-fold coordination and the one appearing around 441 cm^{-1} corresponds to the vibration of the Si-O-Fe bonds. Otherwise, this band around 441 cm^{-1} moves towards higher values and becomes intense, reflecting the formation of ferrosilicates which results from the dissolution of iron oxide in an acidic medium contributing to the polycondensation of porous geopolymer matrix and the removal of impurities within the material.

After the deposition of iron oxide nanoparticles by plasma-assisted hydrolytic precipitation, the intensity of all the absorption bands of the spectrum increases, which could be ascribed to an increase of the oxygen element (in the form of hydroxyl group) after acid activation, plasma-deposition and ageing processes. Otherwise, Kepdieu et al., attributed the intensity bands increase to the high presence of iron oxide within the smectite clay [30]. Some authors have shown that UV radiation emitted in a plasma medium activates the material in the aqueous medium by photo-activation of semi-conductor oxides such as Fe_2O_3, thus leading to high production of O-H [33,34] and hence the obtaining of goethite by oxidation and precipitation according to the Eqs. (5–7).

a) **Oxidation of ferrous ions by the hydroxyl radicals**

$$\boldsymbol{AM \equiv Fe^{2+} + HO^{\cdot} \rightarrow AM \equiv Fe^{3+} + HO^{-}} \quad (5)$$

b) **Precipitation of the ferric ions into iron oxyhydroxide**

$$\boldsymbol{AM \equiv Fe^{3+} + 2HO^{-} + H_2O \rightarrow AM \equiv FeOOH + H_3O^{+}} \quad (6)$$

c) **Precipitation of non-oxidized ferrous ions into iron oxyhydroxide**

$$\boldsymbol{2(AM \equiv Fe^{2+}) + 4HO^{-} \rightarrow 2(AM \equiv FeOOH) + H_2} \quad (7)$$

We could observe a shift of the vibration bands of (T=Si, Al, Fe) T-O-Fe bonds at 441 cm^{-1} towards low values, reflecting the Fe-O stretching and bending vibrations within the volcanic ash material after acid activation. The bands observed around 540 and 420 cm^{-1} also reflect the internal bending vibrations of the Si-O-Si, O-Si-O of SiO_4^+ and $(AlO_4)^{5-}$ bonds within the tetrahedral sites. Breck also explains that bands around 433 cm^{-1}, can be thought of as the pore opening of materials [35]. A slight decrease in the intensity of absorption bands around 433 cm^{-1} is recorded after ageing using a boiling water bath, which can be explained in the same way as Breck by a decrease in volume and porous surface. In addition, ageing of the volcanic ash in a boiling water bath does not change the intensity or positions of the absorption bands. Therefore, FTIR analysis shows the formation of three new bands respectively after acid activation, plasma deposition of FeO_x and ageing by boiling water bath: one around 1048 cm^{-1}, the other around 949 cm^{-1}, and the last around 793 cm^{-1} respectively assigned to the Si-O-T (T= Si, Al, Fe) and Fe-O-OH absorption bands.

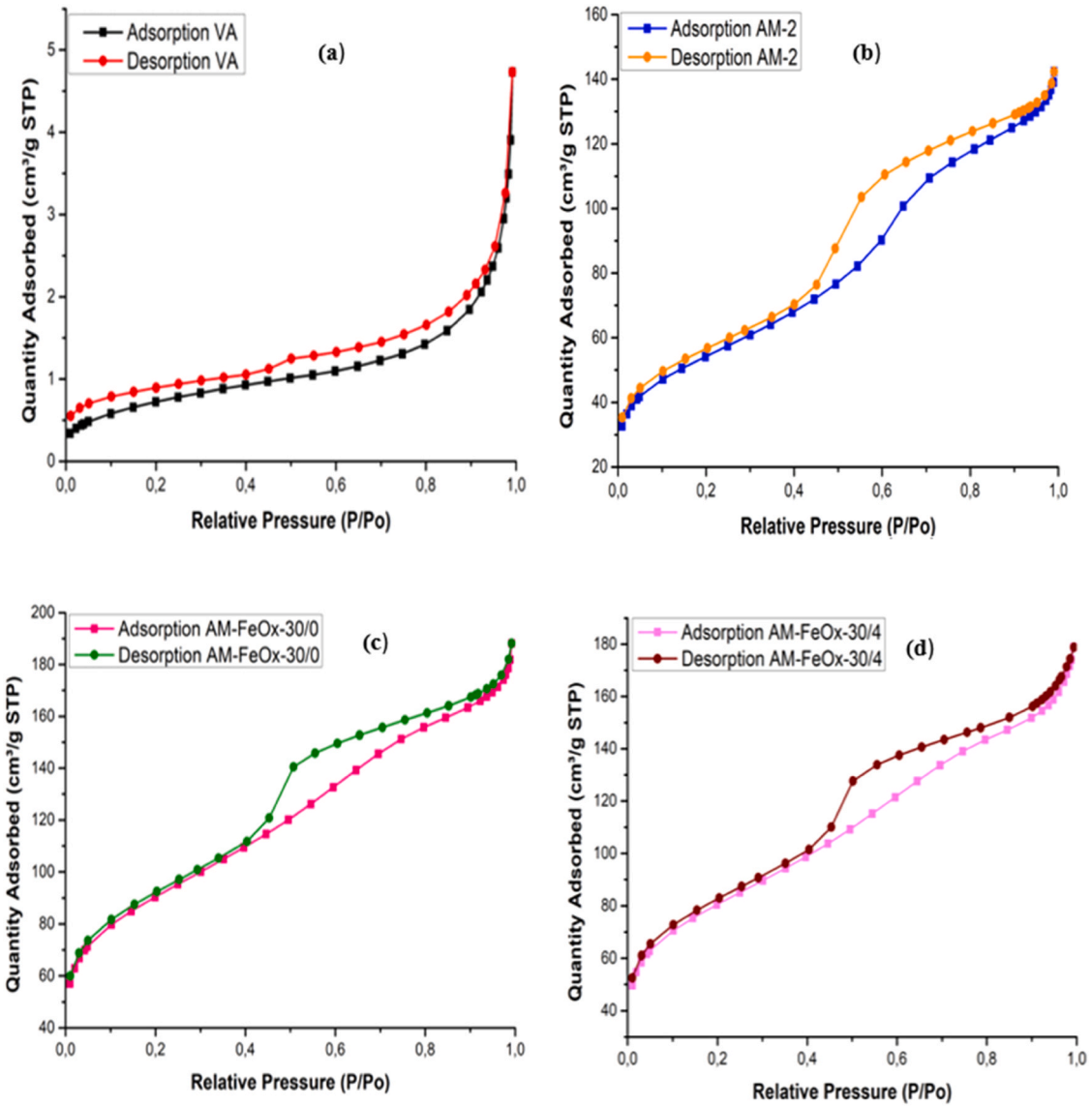

Fig. 4. N_2 adsorption-desorption isotherms of the (a) Raw (VA), (b) Activated (AM-2), (c) Supported (AM-FeOx-30/0), (d) Ageing (AM-FeOx-30/4) materials.

Fig. 3 and Table S2 show the different crystalline phases present in each material revealed by XRD analysis. Among these phases, we found: Anorthite, a sodium disordered (Ca, Na) $(Si,Al)_4O_8$ (PDF: 00–041–1481), Augite $Ca(Mg_{0.7}\ Al_{0.30})(Si_{1.7}\ -Al_{0.30})O_6$ (PDF: 01–078–1392), Maghemite Y-Fe_2O_3 (PDF: 00–039–1346), Hematite-Fe_2O_3 (PDF: 00–033–0664), Wuestite FeO (PDF: 01–089–2468), Silicon Oxide-SiO_2 (PDF: 00–050–1708) and Ferroan Forsterite $Mg_{1.824}\ Fe_{0.176}\ (SiO_4)$ (PDF: 01–083–1541). These data reveal the existence of allotropy of iron in different oxidation states (II and III) within the volcanic ash framework. After chemical (acid) activation, iron-containing minerals, in particular Ferroan forsterite, Hematite, Maghemite and Wuestite, disappeared, but Magnetite was formed Fe_3O_4 (PDF: 01–089–0951). On the one hand, we recorded the disappearance of peaks at 17.4°, 23°, 26,6°, 32,3°, 40°, 39.6°, 38,4°, 52.5°, 61.7°, 57.4° (Ferroan forsterite), 30.5°, 35.7°, 43.1° (Maghemite) 23.7°, 40.61°, 49.9°, 62.4°, 72.1°(Hematite), 60.6°, 35.8°, 60.30° and 72.5° (Wuestite), which can be explained by the non-selective leaching of iron in an acidic environment (Fig. 3b and Table S2) [36,37]. On the other hand, the formation of Magnetite (Fe_3O_4) is ascribed to the reaction between the formed goethite and white Rust ($Fe(OH)_2$ with Rhombohedral structure) according to Eq. 8 [32].

$$2\,\boldsymbol{AM \equiv FeO(OH)} + \boldsymbol{AM \equiv Fe(OH)_2} \longrightarrow \boldsymbol{AM \equiv Fe_3O_4 + 2H_2O} \quad (8)$$

Activated material (AM-2) served as a framework for the deposition of iron particles via gliding arc plasma for 30 min, followed by the ageing for 4 h in a boiling water bath. X-ray pattern (Fig. 3c) shows the formation of new phases after 30 minutes of plasma deposition, namely Labradorite $Ca_{0.68}Na_{0.30}(Al_{1.66}Si_{2.34}O_8)$ with characteristic peaks at 13.8°, 19.1°, 22.11°, 22.9°, 23,7°, 31,6°, 33,89°, 35.8°, 39.2°, 41.1°, 46.1°, 49,8°, 67,4°, 76.4°(2Θ values) (PDF: 01–083–1372), and Sodium Aluminium Silicate $NaAlSiO_4$ at 20,1°, 21.1°, 26,7°, 30.9° and 35.2° (2Θ values) (PDF: 00–033–1203)) (Fig. 3c and Table S2), knowing that Labradorite is a member of Anorthite polymorphism and a mineral of the plagioclase felspar family and tectosilicate subgroup characterized by its albite/anorthite ratio of 30/70 and 50/50. It was found that the X-ray pattern of the material after exposure to plasma and ageing process (Fig. 3d) shows the formation of a dome between 15 and 25° (2θ values) reflecting the existence of an amorphous phase [38,39]. This translates on the one hand, to the generation of an amorphous goethite (AM≡FeOOH) [13]. These results are closely in line with those reported by Tiya and al. [4], where goethite synthesized by plasma-assisted hydrolytic precipitation is revealed on the XRD spectrum through a dome around 20° [4] and confirmed by thermogravimetry and H_2-TPR

Table 1
Textural data of volcanic ash before and after different treatments.

Samples	S_{BET} (m^2/g)	Microporous volume (cm^3/g)	Pore volume (cm^3/g)	Pore diameter D_{BHJ}(Å)
VA	3	0.00	0.01	81
AM−2	188	0.05	0.21	45
AM-FeO_x−30/0	308	0.10	0.28	36
AM-FeO_x−30/4	276	0.08	0.27	36

analyses [4,31,32]. On the other hand, the presence of amorphous aluminosilicate and Iron hydroxide could lead to the obtaining of zeolites through hydrothermal synthesis at low temperatures [38–40]. The ageing of the material increases the intensity of the dome corresponding to the amorphous phase rich in goethite attesting to the deposition of Iron oxide with the sodium Diopside $(Ca_{0.91}Na_{.05}Fe_{0.04})(Mg_{0.90}\ Fe_{0.07}\ Al_{0.03})(Si_{1.97}\ Al_{0.03})O_6$ obtained through the substitution Si^{4+} by Al^{3+} and cationic exchange between $Ca^{2+}$and Na^+, Mg^{2+} and Fe^{2+} [41]. The reactions describing the synthesis of goethite via plasma glidarc route are illustrated through Eqs. (9–11), which present the formation of hydroxyl radicals inducing the oxidation of $AM \equiv Fe^{2+}$ to iron (III) oxyhydroxide (Eq.5) on the aluminosilicate framework of the volcanic ash. After ageing of the plasma-activated material, crystallized silica is observed in the form of SiO_2 quartz at 21°, 26.7, 49.7°, 57.8° and 68.3° (2θ values) (PDF: 01–089–1961) (Fig. 3d) and gives a material with a very high thermal stability.

$$H_2O + e^- \rightarrow H^{\cdot} + HO^{\cdot} + e^- \quad (9)$$

$$H_2O + e^- \rightarrow H^+ + HO^{\cdot} + 2e^- \quad (10)$$

$$AM \equiv Fe^{3+} + 2HO^{\cdot} + H_2O + 2e^- \rightarrow AM \equiv FeOOH + H_3O^+ \quad (11)$$

(AM$\equiv$) represents the framework of the activated volcanic ash containing iron.

The nitrogen (N_2) adsorption-desorption isotherms of the prepared materials are shown in Fig. 4. The three isotherms (Figs. 4b, 4c and 4d) exhibit a hysteresis loop within a relative pressure range (P/P_0) of 0.45–0.95 which is typical of isotherm type IV, illustrating the presence of a mesoporosity after chemical activation, FeO_x plasma-deposition and ageing processes. The shape of the hysteresis loop suggests the presence of closed ink-bottle-shaped pores [42,43]. However, the raw material (VA) shows a weakly marked hysteresis loop at higher relative pressure (Fig. 4a), revealing the presence of a large mesoporosity between particles of a non-porous material [44,45]. We recorded a decrease of the pore diameter at the volcanic ash surface after acid activation, followed by the plasma-deposition of Iron oxide within its framework (Table 1), reflecting an evolution from non-porous material with only interparticular large mesopores (VA) to material with intraparticular mesoporosity. The acid activation of volcanic ash thus significantly creates mesopores and increases the specific surface area (Table 1). Thereby, the appearance of intraparticular mesopores could firstly be explained by the cation exchanges between $Si^{4+} \longrightarrow Al^{3+}$, $Fe^{2+} \longrightarrow Mg^{2+}$, $Al^{3+} \longrightarrow Fe^{2+}$and $Al^{3+} \longrightarrow Fe^{3+}$ which generates more spaces within the tetrahedra, and charge compensation is assured by largest cationic species (Ca^{2+}, Na^+, K^+, H^+…) or medium cationic species (Fe^{3+}, Al^{3+}, Ti^{4+} …) as described through Eq. 12. During the chemical activation, some large cationic species are substituted by smaller ones generating spaces, thus a mesoporosity within the framework. This could also be explained by the acid leaching of basic oxides and other impurities within the raw material (VA).

$$(Si_2O_5, Al_2O_2)n + H_2SO_4 \longrightarrow \underset{\textbf{(Orthothiosialate)}}{n(OH)_3\text{-Si-O-Al}^-\text{-(OH)}_3} \xrightarrow{H_2SO_4} \underset{\textbf{(H}^+\textbf{, Na}^+\textbf{, K}^+\textbf{)-poly(sialate)}}{(H^+, Na^+, K^+)\text{-(Si-O-Al}^-\text{-O)}_n} \quad (12)$$

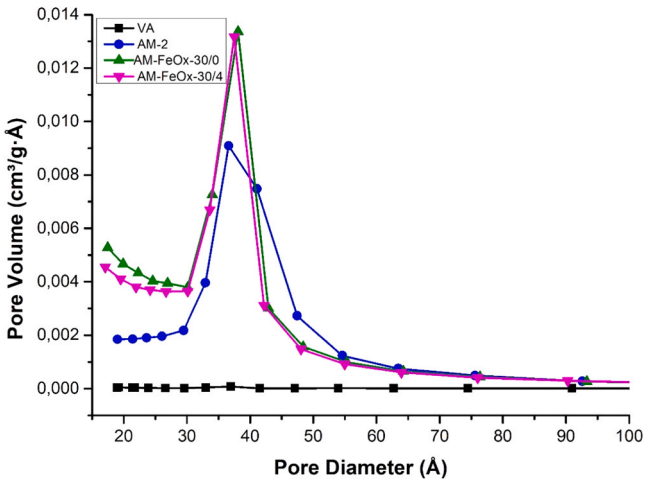

Fig. 5. Distribution of pore sizes of the raw material (VA), activated material (AM-2), supported material (AM-FeOx-30/0) and aged material (AM-FeOx-30/4).

According to Duxson et al., the Davidovits equations developed during the synthesis of alkaline geopolymers in 1991 justify the microstructure, pore distribution and major physical properties of the geopolymer [46]. The current work highlights the fact that volcanic ash as a geopolymer material in a strongly acidic medium undergoes the same phenomena i.e. the microstructure and pore distribution of the volcanic ash. The deposition of iron oxide nanoparticles on AM-2 material (acid-activated volcanic ash) by gliding arc plasma hydrolytic precipitation (Eq.7) considerably increases the specific surface area (S_{BET}) of the material (AM-FeO_x-30/0) (Table 1). A plausible explanation of this increase of the specific surface area could be ascribed to the reduction of particle agglomerations by bombardment of the material surface thanks to the active species (HO$^{\cdot}$, NO$^{\cdot}$, H_2O_2, HOONO….), electrons and/or electric waves generated within the plasma plume, thus leading to the structural reorganization and substitution of Al atom by Fe atom within the tetrahedron of the activated material [17,33,47,48]. In addition, through the presence of hydroxyl radicals and the hydroxyl anion produced by the plasma, oligomers are formed that condense in a three-dimensional (3D) lattice by polycondensation of poly (sialate-siloxo) and poly(sialate-disiloxo) [49] when the Si/Al ratio is above 1. This creation of the network thus increases the specific surface

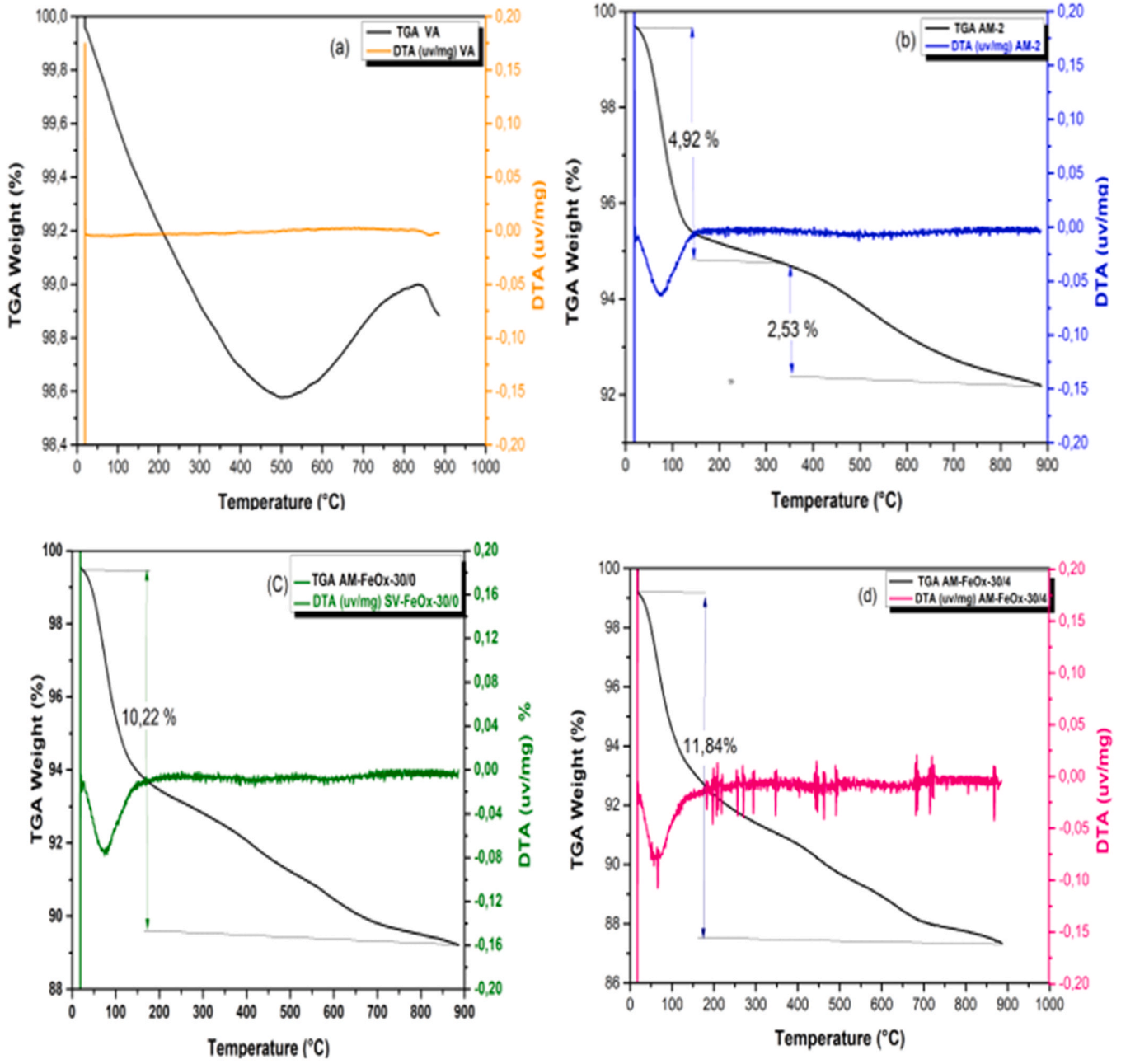

Fig. 6. Thermogravimetric Analyses of different materials (a) Raw (VA), (b) Activated (AM-2), (c) Supported (AM-FeOx-30/0), (d) Ageing (AM-FeOx-30/4) materials.

area, mesoporosity and microporosity. The deposition of FeOx particles via plasma hydrolytic precipitation (described in Figure S4) improves the total pore volume of raw material and confirms Breck's statement mentioned above that the appearance of the IR band at around 433 cm^{-1} corresponds to the opening of the pores within the volcanic ash (VA). After ageing within the boiling water bath, a decrease in the specific surface area (S_{BET}) is recorded, and could be explained, firstly, by the creation of disorder within the network of volcanic ash related to the increase of the amorphous phase (intermediate Augite). Secondly, by the precipitation of ferric and ferrous ions inside the pores of the volcanic ash [6] and the particle's agglomerations due to the shrinkage of the pores after ageing at high temperatures [48]. Therefore, we could say that the specific surface area of acid-activated material highly depends on the applied treatment, composition, and arrangement of the minerals within their crystalline structures. Fig. 5 shows the pores size distribution of the different materials and reveals a monomodal pores

Table 2
Average mass percentage of the chemical elements contained in the different materials obtained by EDX.

Elements	Samples			
	VA Mass (%)	MA-2 Mass (%)	AM-FeO_x-30/0 Mass (%)	AM-FeO_x-30/4 Mass (%)
O	48.3	59	58.1	64.5
Na	1.7	0.2	0.2	0.3
Mg	5.6	0.7	0.3	1.2
Al	6.0	1.4	1.3	1.6
Si	14.8	28.2	28.9	22.8
K	1.1	0.4	0.7	0.5
Ca	6.5	2.9	1.7	3.7
Ti	1.9	1	0.4	0.7
Fe	14.1	1.5	8.7	4.7
S	-	0.3	-	0.2

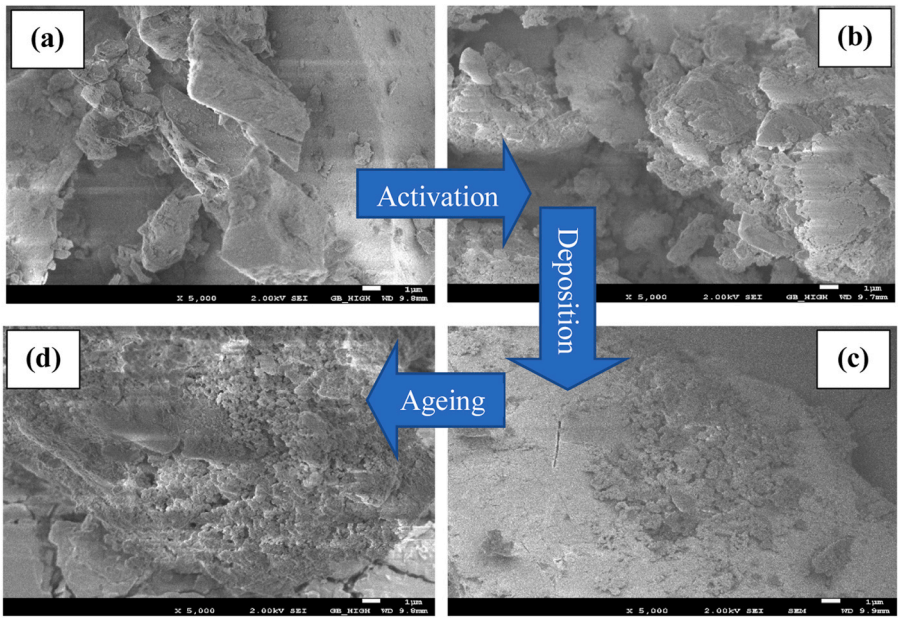

Fig. 7. SEM images at x5000 magnification of (a) Raw (VA), (b) Activated (AM-2), (c) Supported (AM-FeOx-30/0), (d) Ageing (AM-FeOx-30/4) materials.

distribution for AM-2, AM-FeO_x-30/0 and AM-FeO_x-30/4 materials, as marked by the single peak around 38 Å. This peak is within the range of mesoporous materials (but not far to the microporosity range) and corroborates what was previously revealed from the direct analysis of adsorption-desorption isotherms (Fig. 4). On the other hand, the volcanic ash (VA) does not show any peak, thus characterizing its non-porous character, which is confirmed by its isotherm. Figure S5 shows the evolution of the N_2 adsorbed quantities as a function of the treatment applied and illustrates the textural evolution of the raw material (VA). The following evolution of the pore volume (Table 1) AM-FeO_x-30/0 > AM-FeO_x-30/4 > AM-2> VA reflects the evolution of the specific surface area, namely that the chemical activation of VA and deposition of FeO_x by glidarc plasma route, positively modifies its textural properties (specific surface area and porosity).

As compared to the raw material VA (Fig. 6a), Derivative Thermal Analysis (DTA) of AM-2 (Fig. 6b), AM-FeO_x-30/0 (Fig. 6c) and AM-FeO_x-30/4 (Fig. 6d) materials show a single endothermic peak at 75°C corresponding to the removal of bounded or free water [50,51]. Thermogravimetric curves reveal two weight loss stages of 4.9 and 2.5 % respectively within the temperature range of 25–350°C and 350–898°C for acid-activated material (AM-2). After the hydrolytic gliding arc plasma deposition of Iron oxides nanoparticles on activated material framework, an increase of mass loss was observed in one stage between 25 and 898°C. Ageing of the deposited material in a boiling water bath led to further mass loss of 11.8 % compared to 10.2 % for the non-aged material (AM-FeO_x-30/0), but without any change of the temperature range. This slight increase of mass loss can be explained by a gradual opening of the pores in the material after hydrolytic deposition and ageing processes as previously revealed by nitrogen physisorption along an increase of pore volume (Table 1) [36]. The peak of goethite dehydration expected between 250 and 350°C was not observed, but a mass loss of 11.8 and 10.8 % remains not far from the theoretical value (9.9 %) of the dehydration of goethite to hematite according to the Eq. 13. Thus, a predominance of amorphous aluminosilicate phase compared to goethite.

$$2\alpha - FeO(OH) \longrightarrow \alpha Fe_2O_3 + H_2O \quad (13)$$

Energy Dispersive X-ray spectroscopy (EDX) analysis of the volcanic ash (Figure S6a, and Table 2) proves that it mainly contains Oxygen, Silicon, Iron, and Aluminium with an atomic average percentage of 14.1 % for Iron. This quantity is sufficient for heterogeneous Fenton catalysis because previous studies reported that with 2.5–6.8 % by mass of Iron an efficient degradation catalysis was obtained in the Fenton-Like process [4,52]. We also recorded a significant content of Titanium, thus presenting the capital interest of this material in heterogeneous Fenton photocatalysis. However, the existence of an average percentage of 14.8 % for Na, K, Ca, Mg elements within the material could have a strong effect on the accessibility to active sites, and thus the reactivity of volcanic ash. After sulphuric acid-activation of volcanic ash, a decrease of the amounts of these elements was recorded (Table 2) as well as the amounts of Fe and Al. This decrease of mass confirms the above-mentioned statements related to non-selective leaching of Fe and Al, an increase of the specific surface area of the activated material (AM-2) related to the release of active sites. In addition, we record an increase in the quantity of oxygen at the surface of this material (Figure S6b) which confirms the formation of -OH groups and Magnetite through Eq. 8. An increase of the Si/Al ratio from 2.5 to 20.1 is also observed, confirming the formation of the aluminosilicate amorphous within the material during chemical activation. The results of the material supported by the hydrolytic plasma glidarc precipitation confirm the addition of FeO_x compound on the activated material surface. This is

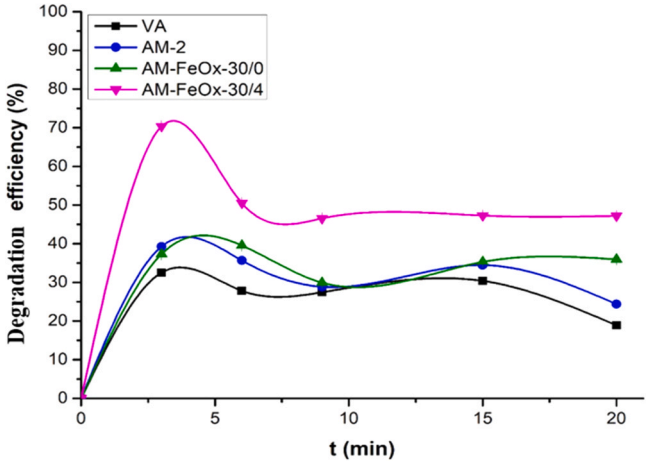

Fig. 8. Influence of the nature of the catalyst as a function of the contact time (pH=3, [Rh6G] = 25 mg/L, [catalyst]=1 g/L, 1 mL of H_2O_2 (30 %)).

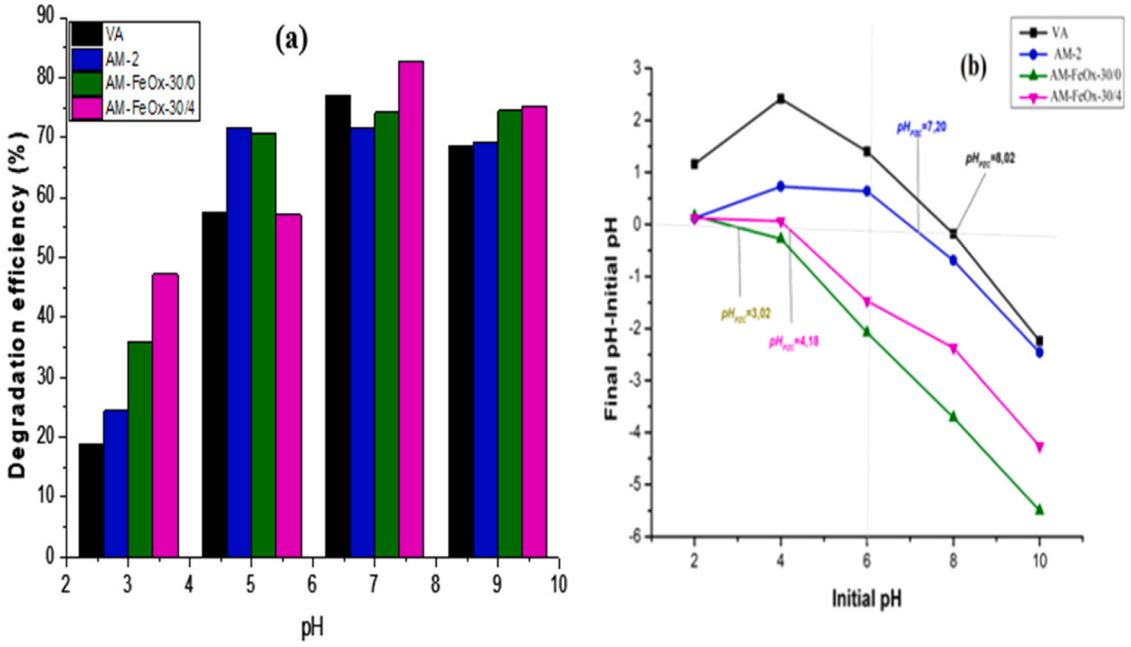

Fig. 9. Evolution of the decolorization degree of Rhodamine 6 G as a function of pH (a) and Point of Zero Charge of different materials (b); [catalyst]=1 g/L; 1 mL H_2O_2 (30 %); [Rh6G] =25 mg, t=20 min).

justified by a variation of the average mass ranging from 1.5 % after activation to 8.7 % after deposition of Iron nanoparticles via hydrolytic precipitation plasma-assisted (Table 2). The increase of the Si/Al ratio from 20.1 to 22.2 after hydrolytic plasma glidarc precipitation confirms the development of the abovementioned 3D network justifying the increase of the meso-microporosity and the specific surface area of the supported material. This report also confirms the thermal stability of the material observed during thermal analyses. On the other hand, there is a decrease of Fe/Al ratio (which ranges from 6.7 for AM-FeO_x-30/0–2.9 for AM-FeO_x-30/4 material). The amount of Iron on the surface of the material obtained after ageing (AM-FeO_x-30/4) decreases (Figure S6d, Table 2), thus confirming the above-mentioned statements, namely that the FeO_x obtained after ageing would have incorporated into the amorphous aluminosilicate phase [13], through substitution of Al by Fe atoms within the mineral's phases (Augite and Sodium Diopsid) and precipitation inside the pores. Hanon and Gaigneaux showed that ageing in the post-discharge process at 100°C increased the number of active species within the nanocomposite's plasma-prepared [53]. Moreover, there is a decrease of the Si/Al ratio after ageing of plasma-supported material (22.2 for AM-FeO_x-30/0–14.3 for AM-FeO_x-30/4), which could be explained by the partial destruction of the network (3D). This corroborates the results of nitrogen physisorption analysis, which described a reduction of the specific surface area and pore volume during the ageing process. The slight presence of sulfur element (S) after sulfuric acid activation of VA could be attributed to the formation of $CaSO_4$ induced by the acid-base reaction between CaO (component the VA) and H_2SO_4. Fig. 7 shows SEM images of prepared materials, where we can see that the morphology of raw material VA is significantly different to the ones of AM-2, AM-FeO_x-30/0 and AM-FeO_x-30/4 materials. VA material reveals large agglomerates particles (Fig. 7a), which move small agglomerates particles after chemical activation (Fig. 7b). The decrease of particles size after acid activation deeply explains the increase of the specific surface area after activation abovementioned (Table 1). Fig. 7c attests the gliding arc plasma-deposition of FeOx on the surface of activated material (AM-2), which seems more homogeneous after ageing at temporal post-discharge at 100°C (Fig. 7d).

3.2. Catalytic activity of different materials

Fig. 8 depicts the evolution of the Fenton catalytic degradation of Rhodamine 6 G (Rh6G) as model pollutant using different prepared materials as catalysts. We could observe an important removal degree of Rh6G after 3 minutes with all prepared materials, which is attributed to the adsorption phenomenon (first stage of the Fenton catalytic route) thanks to the very high availability of adsorption sites. This adsorption is governed on the one hand by interactions between the positively charged (-N+) groups of the Rh6G and negatively charged walls of each material due to the presence of $(AlO_4)^{5-}$ and SiO_3^- groups formed through the substitution of Si^{4+} by Al^{3+} in the three-dimensional network and the insertion of Fe^{2+} within the tetradentate interstices of the aluminosilicates. On the other hand, this can be also explained by a strong attraction between the hydrogen bonds of goethite and the -NH-CH_3 functions of Rh6G. However, the aged material (AM-FeO_x-30/4) reveals a better degradation degree than the plasma-supported (AM-FeO_x-30/0), chemical activated (AM-2), and raw (VA) materials. These results agree with the studies carried out by Boyom et al. in 2020 and Hanon et

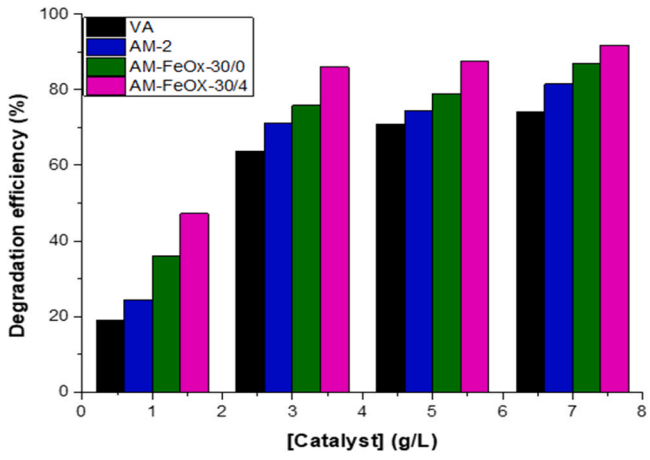

Fig. 10. Degradation of Rhodamine 6 G as a function of catalyst mass ([catalyst]=1; 3; 5; 7 g/L; pH=3; t=20 min, V=50 mL, [Rh 6 G] =25 mg/L).

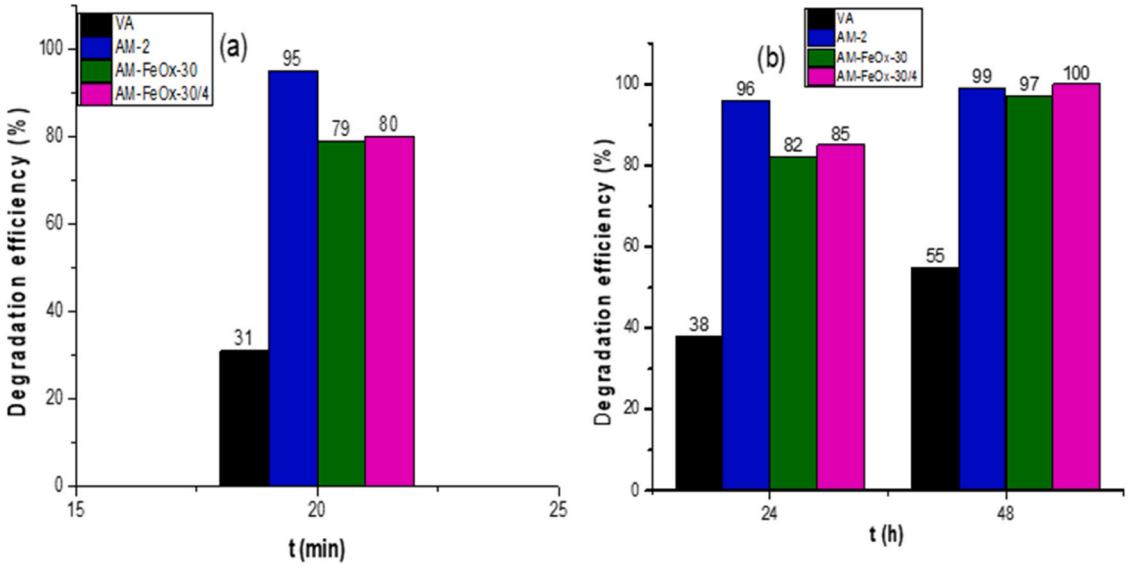

Fig. 11. Effect of volcanic ash activated, supported, and aged decolorization efficiency (pH=7, [catalyst]=3 g/L, t=20 min, [Rh 6 G] =25 mg/L) before (a) and post-treatment (b).

al. in 2024 which prove that the ageing of the material plasma-prepared, impacts its reactivity [48,53]. However, after three minutes of catalytic treatment, we recorded a decrease of degradation degree of Rh6G which is more important with aged material AM-FeO_x-30/4 and stays quasi-constant after five minutes. This evolution may be related to the nature of the pollutant [54]. The tendency curve was obtained by Gondal et al. in 2010 during the sorption and photocatalytic decolorization under monochromatic pulsed laser irradiation of Rhodamine 6 G in aqueous solution with BiOCl and TiO_2 semiconductors as catalysts. Otherwise, we wonder on the real degradation process (or adsorption process only) of Rh6G after 5 minutes of Fenton catalytic treatment, knowing that the pollutant after adsorption could be degraded according to the mechanism illustrated by Eqs. 14–16, due to the presence of iron in the minerals (sodium diopside) and Iron (+III) fixed on the ordered Augite is reduced to Iron (II) according to Eq. 15. However, the raw material (VA) despite its smaller specific surface area reveals non-negligible degradation degree compared to those obtained by the three other materials. This could be attributed to the largest diameter pores (81 Å) of VA (Table 1), allowing a good adsorption of the Rh6G molecule (11Åx16Å) (Figure S1), thus inducing a significant reactivity.

$$\boldsymbol{AM \equiv Fe^{2+} + H_2O_2 \rightarrow AM \equiv Fe^{3+} + HO^{\cdot} + H0^{-}} \quad (14)$$

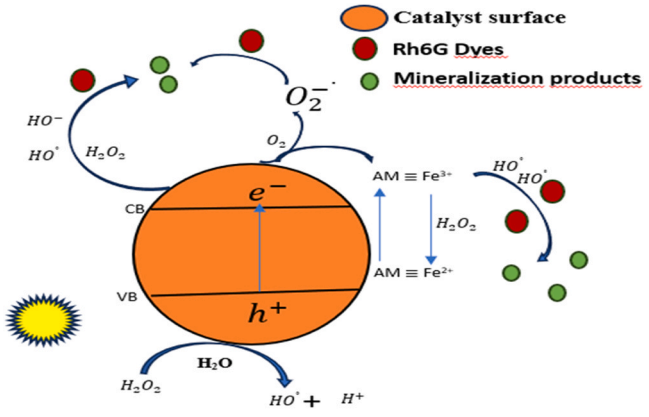

Fig. 12. Mechanism scheme of Fenton catalytic degradation of Rh6G under solar light.

$$\boldsymbol{AM \equiv Fe^{3+} + H_2O_2 \rightarrow AM \equiv Fe^{2+} + HOO^{\cdot} + H^{+} (Slow\ step)} \quad (15)$$

$$\boldsymbol{Rh6G + HO^{\cdot} \rightarrow CO_2 + H_2O + Other\ Mineralization\ Production1} \quad (16)$$

(**AM**〓 Solid surface of the catalyst where the Iron is attached).

3.3. Optimization of operational parameters

The influence of pH solution on the degradation process of Rh6G was studied and the results are shown in Fig. 9. Overall, the catalytic degradation of Rh6G is better for high pH. We can see that the degradation of Rh6G is greater at pH equal to 7 for all the materials. This is justified by the fact that, pH equal to 7 is the optimal pH solution compared to very low pH of solution (pH=3), where the amount of Rh6G removed remains below 27 %. The point of zero charge (PZC) of AM-FeO_x-30/4 material shows that at pH solution below 4.8, its surface is positively charged, thus resulting of the electrostatic repulsion between the surface of AM-FeO_x-30/4 material and the cationic charges of the

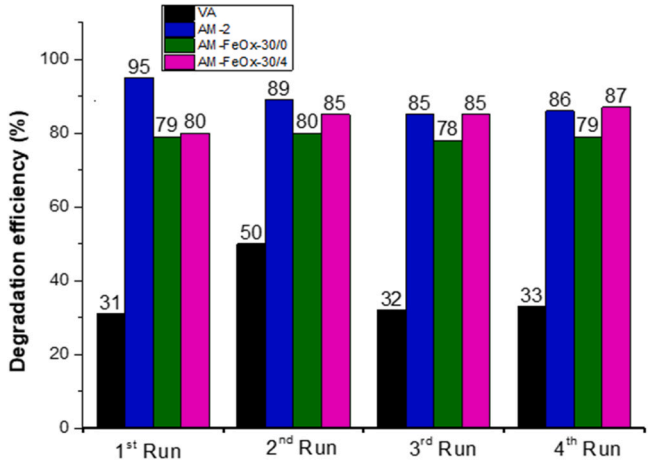

Fig. 13. Study of the catalytic stability of raw, activated, supported and aged volcanic ash during 4 cycles of use of 20 minutes. (pH=7, [Catalyst]=3 g/L, t=20 min, [Rh 6 G] =25 mg/L).

Table 3
Data from iron leaching at different recycling runs for different materials.

	Iron Leached (mmol.L^{-1})			
Run	1	2	3	4
VA	0.003	0.002	0.0005	0
AM−2	0.004	0.003	0	0
AM-FeO_x−30/0	0	0	0	0
AM-FeO_x−30/4	0	0	0	0

Rh6G pollutant, thus inhibiting the catalytic degradation process of Rh6G. On the other hand, for the supported material AM-FeO_x-30/0, the point of zero charge is 3.0 and induces the fact that, when the pH is equal to 3, the surface material is neutral leading to the inhibition of catalytic process. For pH values above 3.0, the surface of the material is negatively charged, resulting in strong degradation efficiency. Activated (AM-2) and raw (VA) materials have respectively PZC values of 7.0 and 8.0, and reflects the fact that, at pH values below 7.0 and 8.0, their respective surfaces of AM-2 and VA are positively charged, thus leading to an electrostatic repulsion between them and the pollutant, resulting in a low adsorption degree and degradation efficiency. On contrary, at pH solution above the PZC values of the activated (AM-2) and raw (VA) materials, their respective surfaces are negatively charged, resulting in an electrostatic attraction between their surfaces and the pollutant molecule positively charged, thus an increase of the degradation efficiency. However, the degradation of Rh6G with activated material (AM-2) at pH below the PZC value of 7.2, in addition to its larger specific surface area value, could be attributed to the Iron leaching in solution reinforcing the Fenton catalytic process. These results deeply highlight the fact that the optimal pH of Fenton catalytic degradation of Rh6G is 7 and the most active material at this pH is the one aged (AM-FeO_x-30/4, PZC=4.2). The influence of catalyst concentration on the degradation efficiency of Rh6G was studied. The results depicted in Fig. 10 show that an increase of the catalyst quantity induces an augmentation of the degradation efficiency, which remains almost constant after a catalyst concentration of 3 g/L. This augmentation is linked to the increase of the adsorption sites number, which leads to a large decomposition of hydrogen peroxide and large production of hydroxyl radicals [7]. Therefore, despite the decrease of the specific surface area of plasma-supported material after ageing, the number of active species increases within the AM-FeOx-30/4 material and degradation of Rhodamine 6 G occurred following the equation reaction (Eq.16). Based on that, we could say that 3 g/L is the optimum catalyst concentration and revealing Rh6G (25 mg/L, pH=7) degradation degrees of 79, and 80 % respectively for AM-FeO_x-0/2 and AM-FeO_x-30/4 after 20 min. Dukkanci et al. in 2010 prepared via hydrolytic precipitation of zeolite composites CuFeZSM-5 as catalysts for Fenton heterogeneous catalytic degradation of Rh6G (100 mg/l, pH=6.5) and reported 100 % of degradation degree after 120 min, with 0.7 mg. L^{-1} of Iron leached in aqueous solution [52]. Tiya et al. in 2018 used volcanic as heterogenous Fenton catalysts for catalytic degradation of Rh6G (25 mg/l, pH=3) and reported 80 % of degradation degree after 120 min, with 0.005 mmol. L^{-1} of Iron leached in aqueous solution [7]. To get a deep understanding of a plausible catalytic degradation of Rh6G after adsorption (previously hypothesized), we envisaged to follow the Fenton catalytic post-treatment of Rh6G during 24 and 48 hours, ie the evolution of the pollutant concentration after the catalyst removal from reaction medium. From the results summarized in Fig. 11, it appears an increase in the degradation degree of Rh6G after 24 hours of post-Fenton catalytic treatment, which is more significant after for 48 hours (Fig. 11b) compared to that obtained during the Fenton catalytic treatment properly (Fig. 11a). Knowing that Rh6G is resistant to biodegradation and photo-degradation [55], this evolution of the pollutant removal during the post-treatment deeply attests the evolution of the degradation process thanks to oxidizing species generated during the Fenton catalytic process. Degradation mechanism of Rh6G illustrated by Fig. 12, shows that in addition to the Fenton catalytic degradation process properly generating powerful oxidizing species such as HO$^{\cdot}$, the photocatalytic degradation of Rh6G occurred knowing that the treatment is carried out in the presence of solar light. Therefore, e^{-} (conduction band) and h^{+} (valence band) photogenerated will respectively react with dissolved O_2 and H_2O via oxidation and reduction to produce other powerful oxidizing species able to mineralize the Rh6G molecules.

3.4. Catalytic recyclability and leaching test

The catalytic stability of prepared materials has been studied along 4 recycling runs. The results depict in Fig. 13 exhibit a high catalytic stability of the supported AM-FeO_x-30/0 and aged AM-FeO_x-30/4 materials, but a slight decrease the efficiency for activated material (AM-2). This is in accordance with the leaching test (Table 3), which shows 0 % of Iron leached after four catalytic runs in solution with the supported and aged materials. A gradual increase of the degradation degree is observed with the aged material, which can be explained by the progressive access of Rh6G by diffusion to the active sites located within the micropores of the amorphous aluminosilicate 3D phase. These results are in accordance with the ones revealed by the EDX analysis (Table 2), which reveals a decrease of active species on the surface of aged AM-FeO_x-30/4 material and is justified by the insertion of these species into the pores and amorphous aluminosilicate. Therefore, we can say that activated volcanic ash is a good porous support for the deposition of Iron nanoparticles through gliding arc plasma route. However, the decrease of the catalytic degradation efficiency of activated material (AM-2) seems to stabilise after the third run and could be ascribed to the evolution of the quantity of Iron leached during the four runs explains this decrease of the degradation efficiency during the use of the activated material (0.004 and 0.003 mmol.L^{-1} leached respectively for the 1st and 2nd runs) (Table 3), reducing its reactivity, which is not the case for the supported and aged materials revealing none Iron leached compared to the leaching reported by Dukkanci et al. in 2010 [52] and Tiya et al. in 2018 [7]. These ferrous and ferric ions in solution in the presence of hydrogen peroxide and the solar light (Eqs.17–21), lead to the production of hydroxyl radicals, followed by the regeneration of the ferrous/-ferric ions and the cycle starts and induces an increase of the catalytic degradation efficiency of Rh6G in aqueous solution [56,57]. This confirms the above-mentioned statements to explain the significant degradation of Rh6G using AM-2 as a heterogeneous photo-Fenton catalyst" (Fig. 9b). On the other hand, the iron (II or III) passing into solution reduces the number of active species on the aluminosilicate support, then leading to the decrease of the performance of the activated material (AM-2). However, the good reactivity and stability of supported and aged materials are ascribed, to better textural properties (specific surface area and pores volume), the presence of mesopores and volcanic ash framework preventing the leaching of Iron oxide in solution.

$$Fe^{3+} + H_2O \rightarrow Fe(OH)^{2+} + H^{+} \quad (17)$$

$$Fe^{3+} + e^{-} + hv \rightarrow Fe^{2+} \quad (18)$$

$$Fe(OH)^{2+} + hv \rightarrow Fe^{2+} + HO^{\cdot} \quad (19)$$

$$Fe^{2+} + H_2O \rightarrow Fe(HO)^{2+} + HO^{\cdot} \quad (20)$$

$$H_2O_2 + hv \rightarrow 2HO^{\cdot} \quad (21)$$

4. Conclusion

Acid activation of volcanic ash followed by the deposition of Iron oxide within the framework of activated material through plasma-assisted hydrolytic oxidation of Fe^{2+} solution, significantly decreases the size of the agglomerate's particles, increases its specific surface area and total pore volume. However, amorphous phases rich in

aluminosilicate and goethite are also formed after plasma-deposition. Ageing of the support material using the water boiling bath leads, on the one hand, to the maturation of the iron particles, thanks to the secondary species such as H_2O_2 (formed by recombination of the primary species), and thus to the substitution of Al atoms by Fe atoms in their tetrahedral sites. On the other hand, to the burial of the amorphous phase and migration (substitution) of the Iron particles towards the network of crystallised minerals, thus a decrease of the specific surface area. Catalytic degradation of Rhodamine 6 G proved that, in addition to be a surface phenomenon, it also depends on the accessibility and reactivity of active iron-rich sites. Post-catalytic treatment of the Rh6G more attests degradation process of the pollutant through the evolution of the pollutant removal. Otherwise, this study has enabled firstly to understand that volcanic ash rich in amorphous goethite is more reactive than the crystallised iron-rich minerals contained in the raw material. Secondly, the valorisation of volcanic ash as local material for a better Fenton catalytic degradation of the organic pollutant.

CRediT authorship contribution statement

Samuel Laminsi: Writing – review & editing, Supervision, Resources, Methodology, Conceptualization. **Elie Acayanka:** Writing – review & editing, Visualization, Investigation. **Franck William Boyom Tatchemo:** Writing – review & editing, Writing – original draft, Visualization, Methodology, Investigation, Data curation. **Mélanie Pitap Mbowou:** Writing – review & editing, Writing – original draft, Methodology, Investigation, Data curation, Conceptualization. **Renaud Cousin:** Writing – review & editing, Resources. **Sebastián Gámez-Rivera:** Writing – review & editing, Investigation, Data curation. **Christophe Poupin:** Writing – review & editing, Investigation, Data curation. **Georges Kamgang Youbi:** Writing – review & editing, Visualization, Investigation. **Eric M Gaigneaux:** Writing – review & editing, Resources.

Declaration of Competing Interest

The authors declare that they have no known competing financial interests or personal relationships that could have appeared to influence the work reported in this paper.

Acknowledgements

We would like to gratefully acknowledge many helpful discussions with Dr. Tiya-Djowe Antoine. We also thanks Éric Genty (University of Littoral-Cote d'Opale) for some characterizations and the MIPROMALO (Mission for the Promotion of Local Materials in Cameroon) for volcanic ash provided.

Appendix A. Supporting information

Supplementary data associated with this article can be found in the online version at doi:10.1016/j.jece.2024.114589.

Data Availability

Data will be made available on request.

References

[1] K. Fuku, H. Kanai, M. Todoroki, N. Mishima, T. Akagi, T. Kamegawa, N. Ikenaga, Heterogeneous Fenton degradation of organic pollutants in water enhanced by combining iron-type layered double hydroxide and sulfate, Chem. Asian J. 16 (2021) 1887–1892, https://doi.org/10.1002/asia.202100375.

[2] X. Zhang, Q. Zhang, T. Yang, Y. Li, J. Li, T. Yu, C. Qu, Research progress of heterogeneous Fenton catalyst for organic wastewater treatment, Environ. Earth Sci. 651 (2021) 042025, https://doi.org/10.1088/1755-1315/651/4/042025.

[3] N. Farhadian, S. Liu, A. Asadi, M. Shahlaei, S. Moradi, Enhanced heterogeneous Fenton oxidation of organic pollutant via Fe-containing mesoporous silica composites, J. Mol. Liq. 321 (2021) 114896, https://doi.org/10.1016/j.molliq.2020.114896.

[4] A. Tiya Djowe, N. Ruth, G. Kamgang Youbi, E. Acayanka, S. Laminsi, E. M. Gaigneaux, FeOx-kaolinite catalysts prepared via a plasma-assisted hydrolytic precipitation approach for Fenton-like reaction, Microporous Mesoporous Mater. 255 (2018) 148–155, https://doi.org/10.1016/j.micromeso.2017.07.036.

[5] N. Miloh, V.K. Kengne, E. Acayanka, P.M. Kouotou, G.Y. Kamgang, Plasma-assisted synthesis of supported superparamagnetic oxides for enhanced Fenton reactions, Water Air Soil Pollut. 235 (2024) 631, https://doi.org/10.1007/s11270-024-07446-1.

[6] A. Tiya Djowe, E. Acayanka, A.P. Mbouopda, F.W. Boyom-Tatchemo, S. Laminsi, E. M. Gaigneaux, Producing oxide catalysts by exploiting the chemistry of gliding arc atmospheric plasma in humid air, Catal. Today 334 (2019) 104–112, https://doi.org/10.1016/j.cattod.2019.01.008.

[7] A. Tiya Djowe, P.N. Lemougna, A. Emadak, M. Pitap Mbowou, S. Laminsi, U. C. Melo, taking advantage of iron contained in natural volcanic ash for catalytic degradation of Rhodamine 6G *Surf*, Interfaces Issn. 3 (2018) 1–3, https://doi.org/10.48442/IMIST.PRSM/jasi-v3i1-3.11169.

[8] N.K. Daud, M.A. Ahmad, B.H. Hameed, Decolorization of Acid Red 1 dye solution by Fenton-like process using Fe–Montmorillonite K10, *Catalyst*, Chem. Eng. J. 165 (1) (2010) 111–116, https://doi.org/10.1016/j.cej.2010.08.072.

[9] J.B. Tarkwa, E. Acayanka, B. Jiang, N. Oturan, G. Kamgang, Youbi, S. Laminsi, M. A. Oturan, Highly efficient degradation of azo dye Orange G using laterite soil as catalyst under irradiation of non-thermal plasma, Appl. Catal. B. 246 (2019) 211–220, https://doi.org/10.1016/j.apcatb.2019.01.066.

[10] H. Hassan, B.H. Hameed, Fe–clay as effective heterogeneous Fenton catalyst for the decolorization of Reactive Blue 4, Chem. Eng. J. 171 (3) (2011) 912–918, https://doi.org/10.1016/j.cej.2011.04.040.

[11] H. Fida, G. Zhang, S. Guo, A. Naeem, Heterogeneous Fenton degradation of organic dyes in batch and fixed bed using La-Fe montmorillonite as catalyst, J. Colloid Interface Sci. 490 (2017) 859–868, https://doi.org/10.1016/j.jcis.2016.11.085.

[12] H. Lim, J. Lee, S. Jin, J. Kim, J. Yoon, T. Hyeon, Highly active heterogeneous Fenton catalyst using iron oxide nanoparticles immobilized in alumina coated mesoporous silica, Chem. Commun. 4 (2006) 463–465, https://doi.org/10.1039/B513517F.

[13] X. Qian, Y. Wu, M. Kan, M. Fang, Do Yue, J. Zeng, Y. Zhao, FeOOH quantum dots coupled g-C_3N_4 for visible light driving photo- Fenton degradation of organic pollutants, Appl. Catal. B. 237 (2018) 513–520, https://doi.org/10.1016/j.apcatb.2018.05.074.

[14] J.N.Y. Djobo, A. Elimbi, H.K. Tchakouté, S. Kumar, Mechanical properties and durability of volcanic ash based geopolymer mortars, Constr. Build. Mater. 124 (2016) 606–614, https://doi.org/10.1016/j.conbuildmat.2016.07.141.

[15] J.N.Y. Djobo, A. Elimbi, H.K. Tchakouté, S. Kumar, Reactivity of volcanic ash in alkaline medium, microstructural and strength characteristics of resulting geopolymers under different synthesis conditions, *J. Mater. Sci.* 51 (2016) 10301–10317, https://doi.org/10.1007/s10853-016-0257-1.

[16] H.K. Tchakoute, A. Elimbi, E. Yanne, C.N. Djangang, Utilization of volcanic ashes for the production of geopolymers cured at ambient temperature, *Cem. Concr. Compos.* 38 (2013) 75–81, https://doi.org/10.1016/j.cemconcomp.2013.03.010.

[17] S.K. Kwon, K. Shinoda, S. Suzuki, Y. Waseda, Influence of silicon on local structure and morphology of γ-FeOOH and α-FeOOH particles, *Corros. Sci.* 49 (2007) 1513–1526, https://doi.org/10.1016/j.corsci.2006.07.004.

[18] J.N.Y. Djobo, A. Elimbi, H.K. Tchakouté, S. Kumar, Mechanical activation of volcanic ash for geopolymer synthesis: effect on reaction kinetics, gel characteristics, physical and mechanical properties, RSC Adv. 6 (2016) 39106–39117, https://doi.org/10.1039/c6ra03667h.

[19] National Toxicology Program,qqww NTP Toxicology and Carcinogenesis Studies of Rhodamine 6G (CI Basic Red 1, CAS No. 989-38-8) in F344/N rats and B6C3F1 mice (feed studies), *Natl. Toxicol.* 364 (1989) 1–192.

[20] G. Dionmbete, N. Miloh, J.-B. Tarkwa, E. Acayanka, A.B.P. Mbouopda, F. W. Boyom-Tatchemo, G.Y. Kamgang, Hybrid composite with lignocellulosic biomass supported titania obtained under plasma conditions for photocatalytic application, Biomass-.-. Conv. Bioref. 14 (2024) 22049–22063, https://doi.org/10.1007/s13399-023-04246-1.

[21] F. Hanon, E.M. Gaigneaux, Synthèse de catalyseurs de type oxydes métalliques simples et mixtes par plasma glidarc à air humide. (2020). ⟨http://hdl.handle.net/2078.1/thesis:23369⟩.

[22] F. Hanon, S. Hermans, E.M. Gaigneaux, What are the species involved in the gliding arc plasma synthesis of heterogeneous catalysts? Catal. Today (2024) 114550 https://doi.org/10.1016/j.cattod.2024.114550.

[23] A.J. Bain, P. Chandna, J. Bryant, Picosecond polarized fluorescence studies of anisotropic fluid media. I. Theory, J. Chem. Phys. 112 (2000) 10418–10434, https://doi.org/10.1063/1.481678.

[24] J.G.S. Van Jaarsveld, J.S.J. Van Deventer, G.C. Lukey, The characterization of source materials in fly ash-based geopolymers. Mater. Lett. 57 (2003) 1272–1280, https://doi.org/10.1016/S0167-577X(02)00971-0.

[25] A. Fernández-Jiménez, A. Palomo, Composition and microstructure of alkali activated fly ash binder: Effect of the activator, Cem. Concr. Res 35 (2005) 1984–1992, https://doi.org/10.1016/j.cemconres.2005.03.003.

[26] J.H. De Boer, B.C. Lippens, B.G. Linsen, J.C.P. Broekhoff, A. Van den Heuvel, T. J. Osinga, Thet-curve of multimolecular N_2-adsorption, J. Colloid Interface Sci. 21 (1966) 405–414, https://doi.org/10.1016/0095-8522(66)90006-7.

[27] L. Guo, K. Zhang, X. Han, Q. Zhao, D. Wang, F. Fu, Y. Liang, Highly efficient visible-light-driven photo-Fenton catalytic performance over FeOOH/Bi_2WO_6 composite for organic pollutant degradation, J. Alloy Compd. 816 (2020) 152560, https://doi.org/10.1016/j.jallcom.2019.152560.

[28] A. Mirzaei, K. Janghorban, B. Hashemi, S.R. Hosseini, M. Bonyani, S.G. Leonardi, G. Neri, Synthesis and characterization of mesoporous α-Fe_2O_3 nanoparticles and investigation of electrical properties of fabricated thick films, *Process. Appl. Ceram.* 10 (2016) 209–217, https://doi.org/10.2298/PAC1604209M.
[29] J.N.Y. Djobo, A. Elimbi, D. Stephan, Phase and dimensional stability of volcanic ash-based phosphate inorganic polymers at elevated temperatures, SN Appl. Sci. 2 (2020) 828, https://doi.org/10.1007/s42452-020-2616-4.
[30] J.M. Kepdieu, C.N. Djangang, G. Tchanang, J.R. Mache, C.F. Abi, P. Blanchart, Kinetic and Mechanism of the Adsorption of ß-Carotene Rich-Palm Oil onto Smectite Clay Activated by Fe (II) Lewis Acid Ion, *J. Chem.* 1 (2022) 1–21, https://doi.org/10.47672/jchem.1284.
[31] H.K. Tchakouté, S. Kong, J.N.Y. Djobo, L.N. Tchadjié, D. Njopwouo, A comparative study of two methods to produce geopolymer composites from volcanic scoria and the role of structural water contained in the volcanic scoria on its reactivity, Ceram. Int. 41 (2015) 12568–12577, https://doi.org/10.1016/j.ceramint.2015.06.073.
[32] Y. Cudennec, A. Lecerf, Étude des mécanismes de formation des oxy-hydroxydes de fer; hypothèses de transformations topotactiques, Comptes Rendus Chim. 6 (2003) 437–444, https://doi.org/10.1016/S1631-0748(03)00069-9.
[33] Hanon, F., Gaigneaux, E.M. The glidarc plasma: an innovative method for the synthesis of heterogeneous catalysts. ⟨https://www.ispc-conference.org/ispcproc/ispc25/pdf/2-A-108⟩.
[34] P.J. Bruggeman, M.J. Kushner, B.R. Locke, J.G. Gardeniers, W.G. Graham, D. B. Graves, G. Zvereva, Plasma–liquid interactions: a review and roadmap, Plasma Sources Sci. Technol. 25 (2016) 053002, https://doi.org/10.1088/0963-0252/25/5/053002.
[35] Breck, D.W. (1974). Zeolite molecular sieves: structure, chemistry, and use.
[36] S.O. Otieno, F.O. Kengara, C.O. Kowenje, R. Mokaya, Hydrothermal synthesis of zeolites using silica extracted from tropical volcanic ash, *Adv. Mater.* 4 (2023) 2292–2300, https://doi.org/10.1039/D3MA00065F.
[37] P.E.A. Lima, R.S. Angélica, R.F. Neves, Dissolution kinetics of metakaolin in sulfuric acid: comparison between heterogeneous and homogeneous reaction methods, *Appl. Clay Sci.* 88 (2014) 159–162, https://doi.org/10.1016/j.clay.2013.12.009.
[38] C. Belviso, M. Abdolrahimi, D. Peddis, E. Gagliano, M. Sgroi, A. Lettino, F. Cavalcante, Synthesis of zeolite from volcanic ash: Characterization and application for cesium removal, Microporous Mesoporous Mater. 319 (2021) 111045, https://doi.org/10.1016/j.micromeso.2021.111045.
[39] C. Belviso, F. Cavalcante, S. Fiore, Synthesis of zeolite from Italian coal fly ash: differences in crystallization temperature using seawater instead of distilled water, Waste Manag. 30 (2010) 839–847, https://doi.org/10.1016/j.wasman.2009.11.015.
[40] C. Belviso, N. Perchiazzi, F. Cavalcante, Zeolite from fly ash: An investigation on metastable behavior of the newly formed minerals in a medium-high-temperature range, Ind. Eng. Chem. Res. 58 (2019) 20472–20480. ⟨https://pubs.acs.org/doi/10.1021/acs.iecr.9b03784⟩.
[41] S. Goldsztaub, Étude de quelques dérivés de l'oxyde ferrique (FeO. OH, FeO_2Na, FeOCl); détermination de leurs structures, Bull. Min. éRal. 58 (1935) 6–76.
[42] S. Lowell, J.E. Shields, M.A. Thomas, M. Thommes, Characterization of porous solids and powders: surface area, pore size and density, SSBM 16 (2012), https://doi.org/10.1007/978-1-4020-2303-3.
[43] M. Thommes, K. Kaneko, A.V. Neimark, J.P. Olivier, F. Rodriguez-Reinoso, J. Rouquerol, K.S. Sing, Physisorption of gases, with special reference to the evaluation of surface area and pore size distribution (IUPAC Technical Report), Pure Appl. Chem. 87 (2015) 1051–1069, https://doi.org/10.1515/pac-2014-1117.
[44] Z.A. ALOthman, A review: fundamental aspects of silicate mesoporous materials, Materials 5 (2012) 2874–2902, https://doi.org/10.3390/ma5122874.
[45] K.S. Sing, Reporting physisorption data for gas/solid systems with special reference to the determination of surface area and porosity (Recommendations 1984), *Pure. Appl. Chem.* 57 (1985) 603–619, https://doi.org/10.1351/pac198557040603.
[46] Z. Yunsheng, S. Wei, L. Zongjin, Composition design and microstructural characterization of calcined kaolin-based geopolymer cement, Appli Clay Sci. 47 (2010) 271–275, https://doi.org/10.1016/j.clay.2009.11.002.
[47] C.F. Mbafou, B. Takam, F.W. Boyom Tatchemo, J.B. Tarkwa, E. Acayanka, G. Y. Kamgang, S. Laminsi, Egg-derived porous plasma modified clay composite for wastewater remediation, Environ. Sci. Pollut. Res. 30 (2023) 6612–6626, https://doi.org/10.1007/s11356-022-22617-5.
[48] F.W. Boyom Tatchemo, F. Devred, S. Laminsi, E.M. Gaigneaux, Temporal post-discharge reactions effect on the oxidative catalytic properties of plasma-synthesized α-MnO_2 nanorods, Appl. Catal. A-Gen. 616 (2021) 118109, https://doi.org/10.1016/j.apcata.2021.118109.
[49] R. Cioffi, L. Maffucci, L. Santoro, Optimization of geopolymer synthesis by calcination and polycondensation of a kaolinitic residue, Resour., Conserve Recycl 40 (2003) 27–38, https://doi.org/10.1016/S0921-3449(03)00023-5.
[50] D.D. Burduhos Nergis, P. Vizureanu, A.V. Sandu, B. Istrate, XRD and TG-DTA Analysis of Fly Ash Based Geopolymer Composite Reinforced with Recycled Glass Fibers, ICIR Eur. Cham: SNS (2023) 31–44, https://doi.org/10.1007/978-3-031-45964-1_4.
[51] C. Nobouassia Bewa, H.K. Tchakouté, D. Fotio, C.H. Rüscher, E. Kamseu, C. Leonelli, Water resistance and thermal behavior of metakaolin-phosphate-based geopolymer cements, J. Asian Ceram. Soc. 6 (3) (2018) 271–283, https://doi.org/10.1080/21870764.2018.1507660.
[52] M. Dükkancı, G. Gündüz, S. Yılmaz, R. Prihod'ko, Heterogeneous Fenton-like degradation of Rhodamine 6G in water using CuFeZSM-5 zeolite catalyst prepared by hydrothermal synthesis, *J. Hazard. Mater.* 181 (2010) 343–350, https://doi.org/10.1016/j.jhazmat.2010.05.016.
[53] F. Hanon, E.M. Gaigneaux, Post-discharge: An interesting step to improve heterogeneous catalysts synthesized by glidarc plasma? J. Chem. Eng. 489 (2024) 151088 https://doi.org/10.1016/j.cej.2024.151088.
[54] M.A. Gondal, X.F. Chang, Z.H. Yamani, UV-light induced photocatalytic decolorization of Rhodamine 6G molecules over BiOCl from aqueous solution, Chem. Eng. J. 165 (2010) 250–257, https://doi.org/10.1016/j.cej.2010.09.025.
[55] M.N. Ghazzal, H. Kebaili, M. Joseph, D.P. Debecker, P. Eloy, J. De Coninck, E. M. Gaigneaux, Photocatalytic degradation of Rhodamine 6G on mesoporous titania films: combined effect of texture and dye aggregation forms, *Appl. Catal. B: Environ.* 115 (2012) 276–284, https://doi.org/10.1016/j.apcatb.2011.12.016.
[56] M.S. Vasilyeva, V.S. Rudnev, A.A. Zvereva, A.Y. Ustinov, O.D. Arefieva, V. G. Kuryavyi, G.A. Zverev, FeOx, SiO_2, TiO_2/Ti composites prepared using plasma electrolytic oxidation as photo-Fenton-like catalysts for phenol degradation, J. Photochem. 356 (2018) 38–45, https://doi.org/10.1016/j.jphotochem.2017.12.007.
[57] R.P. Cavalcante, L. da Rocha Sandim, D. Bogo, A.M.J. Barbosa, M.E. Osugi, M. Blanco, V.S. Ferreira, Application of Fenton, photo-Fenton, solar photo-Fenton, and UV/H_2O_2 to degradation of the antineoplastic agent mitoxantrone and toxicological evaluation, Environ. Sci. Pollut. Res. 20 (2013) 2352–2361, https://doi.org/10.1007/s11356-012-1110-y.